Am J Transl Res 2026;18(2):959-975
www.ajtr.org /ISSN:1943-8141/AJTR0169629

Original Article

Yangxin granules exert cardioprotective effects against acute myocardial infarction by modulating NF-κB to suppress ferroptosis

Guanda Huo[1], Yabin Zhou[1], Zhixin Wu[1], Shude Sun[1], Guanwen Zhu[2], Guangyu Cheng[3], Jiamei Fu[1]

[1]Department of Cardiovascular Medicine, The First Affiliated Hospital of Heilongjiang University of Chinese Medicine, Harbin 150040, Heilongjiang, China; [2]Department of Acupuncture III, The First Affiliated Hospital of Heilongjiang University of Chinese Medicine, Harbin 150040, Heilongjiang, China; [3]Research Center of Traditional Chinese Medicine, The Affiliated Hospital of Changchun University of Chinese Medicine, Changchun 130021, Jilin, China

Received October 29, 2025; Accepted January 6, 2026; Epub February 15, 2026; Published February 28, 2026

Abstract: *Objectives:* To investigate the therapeutic effects of Yangxin granules (YNX), a classic traditional Chinese medicine, in acute myocardial infarction (AMI) and its underlying mechanism. *Methods:* Rats were subjected to left anterior descending coronary artery ligation to establish AMI. Thereafter, YNX was administered once daily for 4 weeks. Cardiac function, histopathological changes, iron deposition, oxidative stress, and ferroptosis related proteins were evaluated. RNA sequencing was performed to identify differentially expressed genes and associated signaling pathways. H9c2 cells were treated with YNX *in vitro* under hypoxic conditions, followed by the supplementation of either a ferroptosis inducer or nuclear factor kappa B (NF-κB) activator. Cell viability, lactate dehydrogenase (LDH) activity, reactive oxygen species (ROS), iron, and ferroptosis and NF-κB pathway related proteins were measured. *Results:* YNX notably enhanced cardiac function, mitigated myocardial injury, alleviated fibrosis, and inhibited iron deposition and oxidative stress in AMI rats. Mechanistically, YNX suppressed ferroptosis by decreasing transferrin receptor 1 (TFR-1) and increasing anti-ferroptotic protein levels. Transcriptomic analysis and western blotting revealed that YNX inhibited NF-κB activity, which was derived from decreased phosphorylation of IκBα and NF-κB p65 inhibitor. *In vitro* assays revealed that 40 μg/mL YNX enhanced H9c2 cell proliferation, decreased LDH, ROS, and iron ion levels, downregulated ferroptosis-related proteins, and inhibited NF-κB pathway activation under hypoxic conditions. These effects were reversed when the cells were treated with a ferroptosis inducer or NF-κB pathway activator. *Conclusions:* YNX alleviates AMI by suppressing ferroptosis by inhibiting the NF-κB pathway, modulating iron metabolism, and mitigating oxidative stress.

Keywords: Yangxin granules, acute myocardial infarction, ferroptosis, NF-κB pathway, traditional Chinese medicine

Introduction

Acute myocardial infarction (AMI) is a life-threatening cardiovascular emergency characterized by coronary artery occlusion that leads to irreversible myocardial ischemic necrosis, which significantly decreases cardiac function and dramatically increases mortality [1]. AMI causes concurrent cardiomyocyte apoptosis, pyroptosis, and necrosis, thereby inducing cardiac dysfunction and progressive heart failure [2-4]. Limited cardiomyocyte regeneration represents the primary constraint on myocardial repair following AMI. Although revascularization and pharmacologic treatments can improve survival outcomes [5-8], they cannot reverse residual cardiac remodeling or regenerative deficits. Therefore, novel therapeutic approaches that promote endogenous repair processes are warranted.

In addition to apoptosis, a well-established form of programmed cardiomyocyte death, ferroptosis has been recently proposed to play a critical role in myocardial injury across multiple cardiovascular pathological mechanisms [9-11]. Ferroptosis is another regulatory mode of cell death with iron-dependent lipid peroxidation [12, 13]. Recently, increasing evidence suggests that ferroptosis plays a role in the patho-

https://doi.org/10.62347/YUKJ5187

physiological mechanisms underlying cardiovascular diseases, as well as in the development of myocardial infarction [14, 15]. For instance, Curdione has been shown to attenuate ferroptosis and protect against isopentenyl disodium induced myocardial infarction by regulating the Keap1/Trx1/GPX4 pathway [16]. lncRNA93358 and ZC3H13 mediated m6A modification attenuates myocardial infarction by inhibiting cell injury, inflammation, oxidative stress, and ferroptosis [17]. Although studies have revealed that alleviating iron-induced myocardial necrosis is essential for maintaining cardiac function, the detailed mechanisms underlying the initiation and progression of ferroptosis at different stages remain unclear.

As an essential transcription factor, nuclear factor kappa B (NF-κB) exerts pivotal effects on cell survival, immunity, and inflammation [18-20]. Furthermore, it modulates inflammatory responses and significantly affects ferroptosis by regulating the expression of genes associated with iron transport, antioxidant mechanisms, and other related pathways [21, 22]. Research suggests that dimethyl fumarate mitigates ferroptosis associated neuroinflammation, oxidative stress, and chronic cerebral hypoperfusion in rats by activating the NRF2/ARE signaling pathway and inhibiting the NF-κB pathway, thereby alleviating cognitive impairment [23]. In addition, FOXO3 upregulates GPX4 and SLC7A11 expression by inhibiting the NF-κB/MAPK pathway, thereby decreasing lipid peroxidation and iron accumulation, subsequently protecting chondrocytes from ferroptotic injury [24]. However, in the context of AMI treatment, the specific role and therapeutic potential of regulating the NF-κB/ferroptosis axis remain unknown. Collectively, modulating the NF-κB signaling pathway to inhibit ferroptosis has emerged as a promising therapeutic strategy to mitigate myocardial ischemic injury.

Traditional Chinese medicine (TCM) has long been used to treat cardiovascular diseases. Yangxin decoction is a well-known TCM formula for the management of such conditions. Yangxin Granules (YNX), derived from this decoction, are widely recognized for improving blood circulation and enhancing myocardial perfusion. From the perspective of TCM, AMI is considered a disorder characterized by blood stasis obstructing heart meridians. TCM emphasizes holistic and personalized management, concentrating on restoring blood circulation and resolving stasis to re-establish the body's balance. YNX can regulate heart rate and rhythm, facilitate unimpeded blood flow, and nourish the entire body. Among the primary components of YNX, *Astragalus* can replenish qi and promote yang, benefiting the defensive qi (Wei) and consolidating the epidermis. Studies have revealed that *Astragalus* preparations exhibit definite therapeutic efficacy in treating AMI, with the ability to inhibit ferroptosis [25, 26]. *Codonopsis,* combined with *Astragalus*, can inhibit inflammation, regulate myocardial energy metabolism, and improve cardiac remodeling while enhancing myocardial contractility [27]. *Wolfiporia extensa* Ginns may prevent cardiac hypertrophy by negatively regulating the Raf/ MEK/ERK pathway [28]; it exerts a supportive effect on assisting treatment with *Astragalus* and *Codonopsis*. *Angelica sinensis*, a traditional medicinal herb, exerts diverse pharmacological effects, including antioxidant, anti-apoptotic, anti-inflammatory, hematopoietic, immunomodulatory, and anti-platelet activities. Previous research has shown that *Angelica sinensis* exerts cardiovascular protective effects in hypertensive heart disease by inhibiting myocardial fibrosis and apoptosis and alleviating oxidative stress [29]. Notably, many herbal components of YNX, including *Astragalus, Codonopsis*, and *Angelica*, exhibit potent anti-inflammatory and antioxidant properties, which are closely associated with the NF-κB pathway and have been implicated in the modulation of ferroptosis [30-32]. This provides a reasonable foundation for the hypothesis that YNX may exert cardioprotective effects via the NF-κB/ferroptosis axis.

Compared with individual monomeric compound administration, TCM can better mitigate the effects of ischemic damage and enhance heart functioning after AMI. Multiple herbs may act synergistically to exert cardioprotective effects while simultaneously modulating multiple biological systems [33-35]. YNX contains various bioactive components that can synergistically interact to regulate iron homeostasis and modulate inflammation signaling cascades. Furthermore, these effects may alleviate myocardial ischemic injury and thereby facilitate cardiac function recovery.

This study aimed to investigate the therapeutic potential of YNX in alleviating AMI-induced car-

diac injury by regulating cardiomyocyte ferroptosis. Based on our transcriptomic data, which suggested the significant involvement of the NF-κB pathway, we focused on evaluating its participation and subsequently developed a new treatment strategy for AMI.

Materials and methods

Materials and reagents

Rat cardiac troponin I (cTnI), aspartate transaminase (AST), and creatine kinase (CK) ELISA kits (Catalog Nos. LJS-E-02539, LJS-E-01860, and LJS-E-03506, respectively) were provided by Wuhan Lingjiesi Biotechnology Co., Ltd. Masson staining kit (Catalog No. BA4079B) was obtained from Zhuhai Baso Biotechnology Co., Ltd. Prussian blue stain kit (Catalog No. G1029) was procured from Servicebio (Wuhan, China). The Cell Counting Kit-8 (CCK-8) cell proliferation and cytotoxicity detection assay kit (Catalog No. HYCCK8-500T) were procured from HYCEZMBIO (Wuhan, China). Malondialdehyde (MDA) assay kit, glutathione assay kit, total superoxide dismutase (SOD) test kit, lactate dehydrogenase (LDH) kit, and serum iron assay kit (Catalog Nos. A003-1-2, A006-2-1, A020-2-2, A001-3-2, and A039-1-1, respectively) were procured from Nanjing Jiancheng Bioengineering Institute (Nanjing, China). Reactive oxygen species (ROS) detection kit (Catalog No. S0033S) was procured from Beyotime (Shanghai, China). Erastin was purchased from GLPBIO (Catalog No. GC16630), and NF-κB activator 1 (NF-κB-Act) was purchased from MedChemExpress (Catalog No. HY-134476). Anti-glutathione peroxidase 4 (GPX4), anti-ferritin heavy chain 1 (FTH1), anti-phospho-NF-κB p65 (Ser536, p-p65), anti-IkK-α, and anti-phospho-IKK-α (Ser180) were procured from Wuhan Lingjiesi Biotechnology Co., Ltd. (Catalog Nos. LJS-D-6701, LJS-D-6278, LJS-A-2006, LJS-A-6012, and LJS-A-3013, respectively). Anti-transferrin receptor 1 (TFR-1) was procured from Abclonal (Catalog No. A5865). Anti-IKBα and anti-phospho-IkB-α (Ser32/36) were procured from ImmunoWay (Catalog Nos. YT2419 and YP0151, respectively). Anti-GAPDH and anti-NF-κB p65 (p65) were procured from Proteintech (Catalog Nos. 60004-1-Ig and 10745-1-AP, respectively). Anti-solute carrier family 7 member 11 (SLC7A11), HRP-Conjugated AffiniPure Goat Anti-mouse IgG (H+L), and HRP-Conjugated AffiniPure Goat Anti-rabbit IgG (H+L) were procured from Boster Biological Technology Co., Ltd. (Catalog Nos. BM5318, BA1051, and BA1054, respectively). Goat anti-Mouse IgG (H+L) Cross-Adsorbed Secondary Antibody (Alexa Fluor™ 594) was procured from Thermo Fisher Scientific (Catalog No. A-11005).

Preparation of YNX and identification of compounds

YNX was purchased from Changchun Xikang Pharmaceutical Co., Ltd. and authenticated by Professor Hong Wei from the Affiliated Hospital of Changchun University of Chinese Medicine. YNX was prepared using a precise combination of 12 herbal ingredients. The composition includes 50 g of *Astragalus membranaceus* (Batch No.: C3012403003), 15 g of *Codonopsis pilosula* (Batch No.: C2602403-003), 15 g of *Wolfiporia extensa* (Batch No.: C0452404006), 15 g of *Wolfiporia extensa* Ginns (*Wolfiporia cocos* sclerotium with pine root, Batch No.: C0472404003), 20 g of *Angelica sinensis* (Batch No.: C2592403005), 15 g of *Pinellia ternate* Breit (Batch No.: DC0022401003), 15 g of *Ophiopogon japonicus* Ker Gawl (Batch No.: C1192404004), 15 g of *Schisandra chinensis* Baill (Batch No.: C1892402001), 10 g of *Cinnamomum cassia* J.Presl (Batch No.: C1452403001), 10 g of *Platycodon grandifloras* A.DC. (Batch No.: 240401482), 10 g of *Cimicifuga foetida L.* (Batch No.: 2404001), and 20 g of *Polygala tenuifolia* Willd. (Batch No.: 2403001). All plant names were checked with MPNS (http://www.mpns.kew.org) on July 2, 2025. A decompression drying process was utilized to powder the herbs. Briefly, 10 times the volume of water was added, followed by decoction two times, each time for 1.5 h. The decoctions were combined and concentrated to a relative density of 1.20-1.25. Decompression drying was performed at 70°C, followed by crushing the dried extract to obtain the powdered medicine. Botanical nomenclature was verified via http://www.worldfloraonline.org (accessed: July 2, 2025).

Liquid chromatography-mass spectrometry (LC-MS) was performed to characterize the principal chemical components of YNX. Chromatographic separation was achieved using the Vanquish UHPLC system with the Hypersil Gold C18 analytical column. MS analysis was performed using the Agilent 6545 Q-TOF mass

spectrometer with the Dual AJS electrospray ionization source, operating in both positive and negative ionization modes with alternating polarity acquisition.

Preparation of animal model and drug administration

Six- to eight-week-old adult male Sprague Dawley rats weighing 180-220 g were acquired from SPF (Beijing) Biotechnology Co., Ltd. [production license number: SCXK(Jing)2024-0001]. The rats were housed under controlled condition (temperature, 25°C ± 2°C; relative humidity, 55% ± 5%) with a 12-h light/dark cycle and *ad libitum* access to water and food. Rats were adaptively fed for 1 week. The welfare of experimental animals was ensured based on the Laboratory Animal - Guideline for Ethical Review of Animal Welfare (GB/T 35892-2018). The study protocol was approved by the Animal Ethics Committee of Changchun University of Chinese Medicine (Approval No. 2024859).

To establish an AMI rat model, the left anterior descending coronary artery was ligated. Briefly, rats were anesthetized by intraperitoneally injecting 1% pentobarbital sodium (40 mg/kg) with mechanical ventilation using a small animal ventilator. The 3rd-4th costal thorax of the left sternal margin was opened, and the left main coronary artery was located. A 2 mm needle was inserted underneath the left atrial auricle. Thereafter, a 6-0 silk wire was utilized to ligate the left anterior descending branch. ST-segment elevation by over 0.2 mV indicated successful model establishment. To clarify the functions of YNX, all AMI rats were randomly divided into five groups (6 rats/group): sham, AMI, low-dose YNX (YNX-L), high-dose YNX (YNX-H), and enalapril (positive control) groups. The rats in the sham group underwent the same operation but without coronary artery ligation. The equivalent gavage dose for rats was calculated by normalizing body surface area. Specifically, the clinically recommended dose for a 70 kg adult is 210 g/day. Considering that the gavage dose for rats is approximately 6.3 times higher than that for humans, the equivalent gavage dose for rats was determined to be 18.9 g/kg/day. Consequently, the gavage doses for rats in the YNX-L and YNX-H groups were 9.45 and 18.9 g/kg, respectively. For enalapril (Macklin, E830566-1g), the recommended clinical dose is 20 mg/day, and the equivalent gavage dose in rats is 1.8 mg/kg. Twenty-four hours after the surgery, rats were administered the drug according to the aforementioned protocol, once daily. Four weeks after drug administration by gavage, all rats were sacrificed via anesthesia. Peripheral blood and myocardial tissues were collected and stored in liquid nitrogen for further analysis.

Echocardiographic assessment

All rats were subjected to echocardiographic evaluation at 4 weeks post-model induction. After anesthesia with intraperitoneal administration of pentobarbital, the rats were prepared for surgery by shaving and sterilizing the left anterior thoracic region with povidone-iodine. Transthoracic echocardiography was performed to measure cardiac function and the ventricular dimensions of the rat hearts. A two-dimensional ultrasound was used to measure the following parameters in the parasternal long-axis view via M-mode echocardiography: left ventricular end-diastolic diameter (LVEDD), left ventricular end-systolic diameter (LVESD), increased left ventricular ejection fraction (LVEF), and left ventricular fractional shortening (LVFS). Mean values were obtained by averaging three serial measurements. All measurements were undertaken by a sonographer blinded to this study.

Measurement of cardiac injury markers

Rat serum samples were obtained to evaluate the changes in key cardiac function biomarkers, including cTnI, CK, and AST.

Histopathological analysis of myocardial tissue

All rats were sacrificed after terminal echocardiographic assessments. Cardiac tissues were immediately harvested and stored in 10% neutral buffered formalin before histopathological analysis. Cardiac tissues were prepared into 4-μm paraffin sections at the left ventricular level to perform the following three staining methods.

Hematoxylin and eosin (H&E) staining was performed for general morphological evaluation. Sections were deparaffinized in xylene and rehydrated using a graded ethanol series (100% to 70%). Nuclei were stained with

Harris's hematoxylin for 5 min, followed by rinsing in tap water for 10 min and differentiation with 1% acid alcohol. Cytoplasmic counterstaining was performed with Eosin Y for 1-3 min. After dehydration using an ethanol series and xylene clearance, slides were mounted with neutral resin. A bright-field microscope was used to observe myocardial cellular morphology and general tissue structure.

To quantitatively evaluate myocardial collagen deposition, tissue sections were deparaffinized and subjected to Masson's trichrome staining protocols. Specifically, sections were incubated with Weigert's iron hematoxylin for nuclear staining for 10 min, followed by rinsing with tap water, staining with Lichun red acid fuchsin dyeing solution for the cytoplasm and myocyan fiber for 5 min, and differentiating with 1% phosphomolybdic acid solution for 5 min. After staining with aniline blue for 5 min to differentiate the collagen fibers, the sections were dehydrated through graded ethanol, cleared in xylene, and mounted with resin, resulting in blue-stained collagen fibers. Cardiomyocytes and erythrocytes could be viewed as red cells under a bright-field microscope.

Prussian blue stain was used to assess iron deposition. This method specifically detects the presence of ferric iron (Fe^{3+}). Briefly, sections were incubated with a Prussian blue working solution for 1 h at room temperature, followed by two washes with distilled water. Nuclei were counterstained with 0.1% nuclear fast red for 5 min. After dehydration and mounting, a bright blue granule indicated the presence of Fe^{3+} deposits within cardiomyocytes or interstitial regions.

Immunofluorescence (IF) staining

Paraffin sections were dewaxed and hydrated, followed by microwave heat-induced antigen retrieval using citrate buffer. After serum blocking, the sections were incubated overnight with the primary anti-p-p65 antibody (1:200) at 4°C. Subsequently, the sections were incubated in the dark at room temperature with the Alexa Fluor™ 594 fluorescein-labeled Goat anti-Mouse IgG (H+L) secondary antibody (1:500) for 1 h. The cell nuclei were counterstained with DAPI. Finally, the sections were sealed with an anti-fluorescence quenching agent. All images were observed and acquired under a fluorescence microscope (Nikon, ECLIPSE Ci).

RNA sequencing

RNA was extracted from rat myocardial tissues of the sham, AMI, and YNX-H groups according to the instructions. Total cellular RNA was extracted using TRIZOL regent. Then, RNA purity, quantity, and quality were measured using a Nano Drop spectrophotometer and an Agilent bioanalyzer. Thereafter, a sequencing library was constructed. DNBSEQ-T7 was applied to sequence the sequencing library in a PE150 model by Wuhan Lingsi Biotechnology Co., Ltd. (Wuhan, China). All reads were subjected to strict quality control to remove low-quality reads. Then, detailed bioinformatic analyses were conducted.

Cell culture and treatment

Rat embryonic ventricular myocytes (H9c2) were purchased from American Type Culture Collection and cultured in Dulbecco's modified Eagle medium at 37°C, 5% CO_2. For the myocardial ischemia mimic, the cells were cultured in a glucose-free and serum-free medium for 18 h under hypoxia (5% CO_2, 94% N_2, and 1% O_2).

After treating the cells with varying concentrations (0, 5, 10, 20, 40, 80, 100 μg/mL) of YNX for 6 h, the model was constructed as described above. Subsequently, the CCK-8 assay was performed to evaluate cell proliferation, whereas the LDH assay was performed to measure LDH levels, which determined the optimal concentration of YNX at 40 μg/mL.

H9c2 cells were randomly divided into the following groups: control, hypoxia, YNX (40 μg/mL), YNX (40 μg/mL) + Erastin (5 μM [36], a ferroptosis activator), and YNX + NF-κB-Act (5 μM [37], a NF-κB activator). All groups, except for the control group, received hypoxia treatment.

CCK-8 assay

Briefly, 5 × 10^3 H9c2 cells/well were plated in a 96-well plate. A blank control group was set up, followed by overnight incubation at 37°C. Then, according to the experimental groups and treatment methods, cells were treated with different YNX doses for 6 h at 37°C and 5% CO_2. Thereafter, in glucose-free and serum-free medium, cells were subjected to hypoxic conditions (1% O_2, 5% CO_2, 94% N_2) for 18 h. Cell

viability was determined using the CCK-8 assay kit at designated time points according to the manufacturer's instructions. The cells were treated with CCK-8 solution for 2 h, followed by absorbance measurements at 450 nm using a microplate reader.

Detection of LDH, MDA, SOD, and GSH contents

Serum samples and cells were centrifuged (3,000 rpm, 4°C) for 10 min to collect supernatants. MDA, LDH, SOD, and GSH contents were measured using commercial kits according to the manufacturer's protocols.

ROS measurement

After centrifugation of cells at 3,000 rpm for 10 min, the supernatants were discarded. The harvested cells were resuspended in serum-free medium supplemented with 10 μM DCFH-DA (dilution, 1:1,000) at a density of 1×10^5 cells/ml before an additional 20 min of incubation at 37°C, with mild agitation at 3-5-min intervals. Unincorporated probes were removed by washing the cells twice with phosphate-buffered saline (PBS). Fluorescence intensity was quantified using the PerkinElmer EnVision microplate reader. Data analysis was subsequently conducted based on the obtained fluorescence values.

Iron measurements

Serum samples were centrifuged at 3,000 rpm for 10 min, and the supernatants were collected for analysis. Tissue homogenates were prepared by washing the tissues with cold PBS (0.01 M, pH 7.4), followed by tissue homogenization in PBS using a tissue grinder on ice and centrifugation again at 3,000 rpm for 10 min to yield supernatants. Commercial kits were used to measure iron concentrations. Serum iron levels were measured by incubating diluted samples and standards with an iron chromogenic reagent at 95°C for 5 min, followed by centrifugation, and absorbance was measured at 520 nm using a microplate reader. Tissue iron levels were similarly measured. Iron contents were normalized to total protein levels, which was determined using the BCA assay. Standard curves for iron quantification were generated using iron standards provided by the manufacturer. Iron levels were computed using the corresponding regression equations. The final iron concentrations were expressed in μmol/L for serum samples or in μmol/g protein for tissue samples.

Western blotting

RIPA lysis buffer supplemented with protease/phosphatase inhibitors was used to extract protein samples from H9c2 cells and rat myocardial tissues. Total protein concentrations were measured using the BCA assay. After 15 min of protein denaturation with 5× reducing SDS loading buffer at 95°C, protein aliquots (40 μg/lane) were subjected to SDS-PAGE using 5% stacking and 10%-12% resolving gels for separation under constant voltage (75 V for stacking and 120 V for resolving). The proteins were transferred onto PVDF membranes using a wet transfer system. After blocking with 5% skim milk in TBST and overnight incubation with primary antibodies at 4°C (GAPDH, 1:10,000; GPX4, FTH1, SLC7A11, 1:1,000; TFR-1, 1:5,000; p65, 1:3,000; p-p65, 1:1,000; IkK-α, 1:1,000; p-IkK-α, 1:1,000; IκB-α, 1:1,000; and p-IκB-α, 1:1,000), the membranes were incubated with HRP-labeled secondary antibody (1:10,000) under ambient temperature for 1 h. An ECL substrate was used to visualize protein signals. Band intensities were quantified via grayscale analysis.

Statistical analysis

All results were expressed as mean ± SEM. GraphPad Prism version 9.3.0 was used for statistical analysis. Between-group and among-group differences were compared using the unpaired Student's t-test and one-way analysis of variance plus Bonferroni's post-hoc test, respectively. A p-value of <0.05 indicated significant differences.

Results

UPLC-MS analysis of the prototype components of YNX

The prototype components of YNX were comprehensively characterized via UPLC-MS/MS analysis based on an original database, in which the quality database was constructed based on reference standards and the metDNA2 platform. In total, 1,464 metabolites (782 metabolites in the positive ion mode and 682

metabolites in the negative ion mode) were detected and identified (**Figure 1A**, **1B**). The prominent chemical classes contributing to the metabolic profile of YNX were as follows: 247 terpenoids, 181 fatty acids, 144 alkaloids, 144 flavonoids, and 29 carbohydrates. Among them, flavonoids, terpenoids, and alkaloids may serve as the effective active ingredients of YNX for treating AMI, as these compounds exhibit a broad spectrum of biological activities, including antioxidant, anti-inflammatory, vasodilatory, and cardioprotective properties.

YNX treatment enhanced cardiac function in the AMI rat model

To determine the essential role of YNX in improving cardiac function after myocardial infarction, rat hearts were harvested for additional experiments after modeling and treatment. The echocardiograms of the rats in each group were obtained via cardiac color Doppler ultrasound (**Figure 2A**). The findings suggested that compared with the AMI group, the YNX group had smaller LVEDD and LVESD (**Figure 2B**, **2C**). In contrast, YNX treatment significantly increased LVEF and LVFS (**Figure 2D**, **2E**). H&E staining (**Figure 2F**) revealed significant myocardial injury in the AMI group, and treatment with YNX partially alleviated these injuries. Consistently, Masson's trichrome staining (**Figure 2G**) revealed that YNX notably delayed myocardial fibrosis progression.

Next, we measured serum cTnI, CK, and AST levels in each group (**Figure 2H-J**). YNX dosing dependently prevented the elevation of these three indices in rats with AMI.

Regulatory effect of YNX on myocardial ferroptosis in rats

Next, we investigated the anti-ferroptotic mechanisms of YNX by determining the changes in myocardial iron metabolism. Positive Prussian blue images revealed significant iron deposits (blue granule) in the myocardial tissues of rats in the model group, which was significantly reduced after YNX treatment (**Figure 3A**). We further examined iron ion levels in rat myocardial tissues (**Figure 3B**) and serum (**Figure 3C**). We observed that YNX administration significantly reduced the degree of iron ion-induced cell death in AMI rats. Western blot analysis of heart tissue proteins from each group (**Figure 3D-H**) revealed that TFR-1 levels were significantly increased, whereas FTH1, GPX4, and SLC7A11 levels were significantly decreased in rat hearts after AMI. In contrast, YNX administration significantly decreased TFR-1 levels and restored FTH1, GPX4, and SLC7A11 levels. Consistently, serum analyses showed that, compared with the AMI group, LDH and MDA levels were significantly decreased (**Figure 3I**, **3J**) while SOD and GSH levels were significantly increased (**Figure 3K**, **3L**) in the YNX group. Collectively, these data suggest that YNX can effectively decrease ferroptosis in rat myocardial tissues after infarction. Furthermore, the efficiency of ferroptosis inhibition was better in the high-dose group than in the low-dose group.

Transcriptomics analysis to elucidate the mechanism of YNX on AMI

To further explore the regulatory mechanism underlying YNX in cardiac function in post-infarction rats, myocardial tissues were collected from rats in the sham, AMI, and YNX-H groups for RNA-seq analysis. Transcriptome profiling revealed that 1,700 genes were upregulated, whereas 539 were downregulated in the AMI group compared with the sham group (**Figure 4A**). In contrast, 419 genes were upregulated and 266 were downregulated in the YNX-H group compared with the AMI group (**Figure 4D**). Subsequently, Gene Ontology (GO) (**Figure 4B**, **4E**) and Kyoto Encyclopedia of Genes and Genomes (KEGG) enrichment (**Figure 4C**, **4F**) analyses were conducted. GO enrichment analysis of the differentially expressed genes in the two pairs of sample sets revealed that both sets were enriched in the inflammatory response-related biological processes. KEGG pathway enrichment analysis revealed that both sets were enriched in the NF-κB signaling pathway. Evidently, the NF-κB signaling pathway is a well-established signaling pathway to regulate inflammatory responses. Based on these findings, we hypothesize that YNX can enhance cardiac function in post-infarction rats by regulating the NF-κB pathway.

NF-κB pathway activation in rat myocardial tissues

To verify whether YNX can modulate the NF-κB pathway, myocardial tissues from each rat group were subjected to western blotting and IF

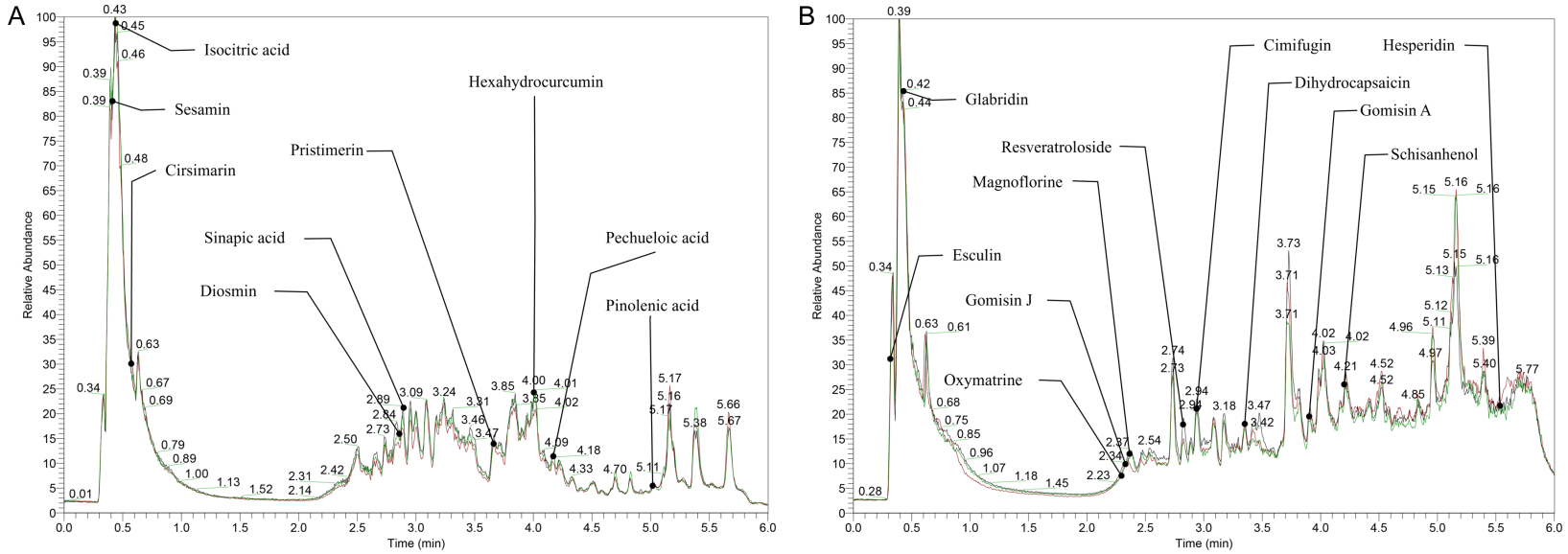

Figure 1. Total ion chromatograms (TICs) of YNX. A. TICs of YNX in positive ion mode; B. TICs of YNX in negative ion mode.

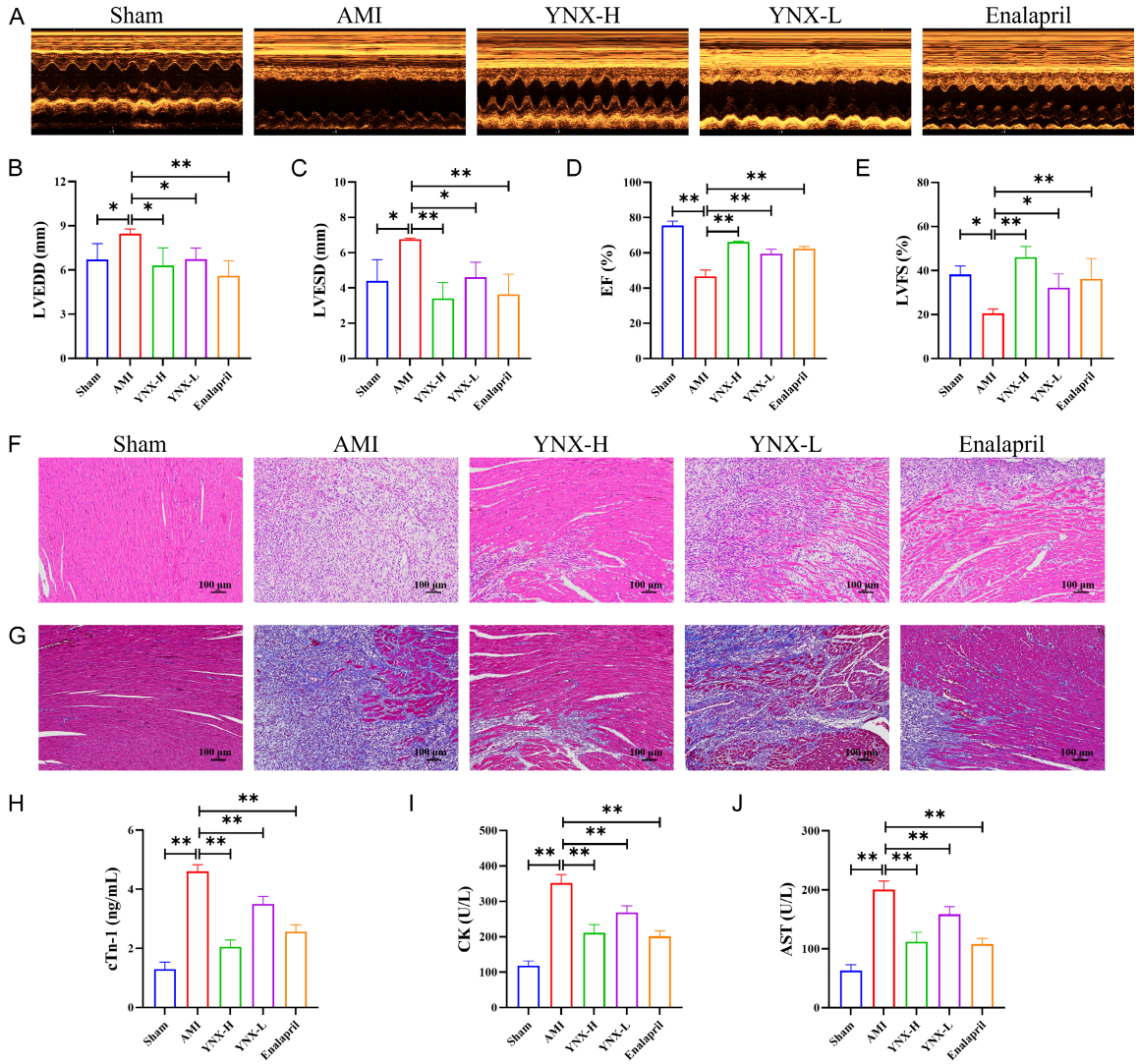

Figure 2. Cardiac function assessments in rats. A. Representative echocardiographic images from each group; B-E. Quantitative analysis of LVEDD, LVESD, LVEF, and LVFS; F. H&E staining for evaluation of myocardial injury (scale bar = 100 μm); G. Masson's trichrome staining for evaluation of myocardial fibrosis (scale bar = 100 μm); H-J. Biochemical analyses of serum cardiac injury markers, including cTnI, CK, and AST. Notes: LVEDD, left ventricular end-diastolic diameter; LVESD, left ventricular end-systolic diameter; LVEF, left ventricular ejection fraction; LVFS, left ventricular fractional shortening; cTnI, cardiac troponin I; CK, creatine kinase; AST, aspartate aminotransferase. Data are expressed as mean ± SEM (n = 6). **P*<0.05, ***P*<0.01.

analysis. Western blotting (**Figure 5A-D**) revealed a marked decrease in p-IκKα, p-IκBα, and phosphorylated p65 subunit (p-p65) levels in the YNX group compared with the AMI group. Consistently, IF analysis (**Figure 5E**) revealed that YNX administration markedly reversed the nuclear translocation of p-p65 induced by myocardial infarction. Collectively, these findings suggest YNX administration effectively attenuates the activation of the NF-κB pathway. The high-dose group exhibited a more pronounced effect than the low-dose group.

Effect of YNX on an H9c2 cell model of AMI

To further investigate the mechanism of YNX in alleviating myocardial infarction *in vitro*, a hypoxia-induced myocardial injury model was established using H9c2 cells. CCK-8 and LDH assays, along with western blotting were performed to evaluate the effects of YNX. The CCK-8 and LDH assays (**Figure 6A**, **6B**) revealed that YNX exerted optimal effect at a concentration of 40 μg/ml. After measuring intracellular iron contents (**Figure 6C**), we observed that

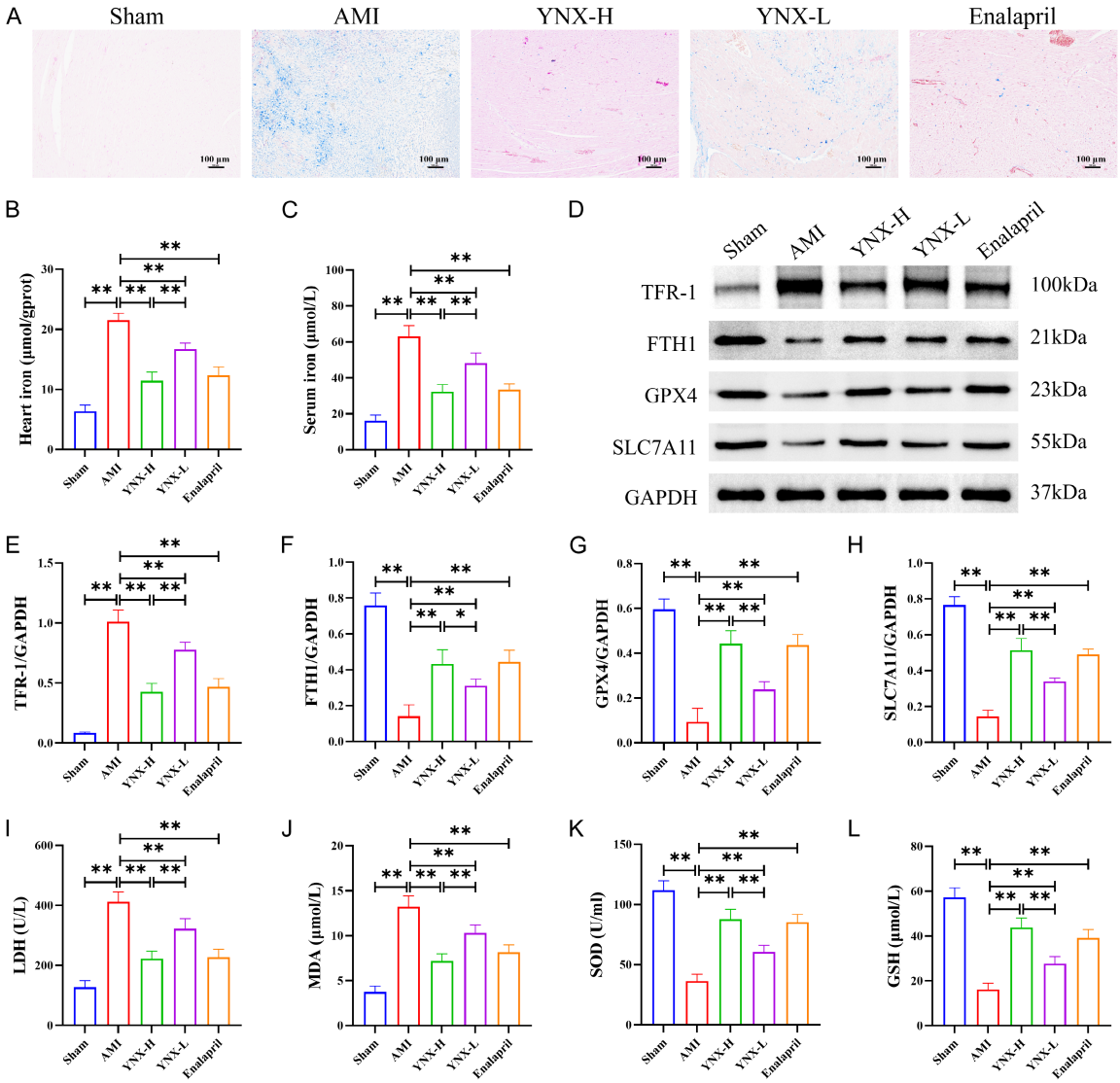

Figure 3. Assessment of ferroptosis in rats. A. Prussian blue staining showing iron ion deposition in rat myocardial tissues (scale bar = 100 μm); B. Quantification of ion concentration in rat myocardial tissues; C. Serum ion levels in rats; D-H. Western blotting and quantitative analysis for detecting the expression levels of TFR-1, FTH1, GPX4 and SLC7A11 in rats across groups; I-L. Measurement of serum LDH, MDA, SOD, and GSH levels. Notes: TFR-1, transferrin receptor-1; FTH1, ferritin heavy chain 1; GPX4, glutathione peroxidase 4; SLC7A11, solute carrier family 7 member 11; LDH, lactate dehydrogenase; MDA, malondialdehyde; SOD, superoxide dismutase; GSH, glutathione. Data are expressed as mean ± SEM (n = 6). **P*<0.05, ***P*<0.01.

YNX administration, to some extent, reduced the elevated iron levels induced by hypoxia. Furthermore, by detecting the ferroptosis-related indices in cells (**Figure 6D-G**), we noted that compared with the hypoxia group, ROS, MDA, and LDH levels were significantly decreased, whereas GSH levels were increased in the YNX group. Nevertheless, the inhibitory effect of YNX on ferroptosis was repressed after incubation with the ferroptosis inducer erastin or the NF-κB activator. In addition, western blotting (**Figure 6H-M**) revealed that YNX significantly decreased TFR-1 levels, increased FTH1, SLC7A11, and GPX4 protein levels, and inhibited NF-κB pathway activation, compared with the hypoxia group. However, co-treatment with the ferroptosis activator erastin or NF-κB activator reversed the abovementioned effects of YNX.

Discussion

AMI remains a life-threatening cardiovascular disease, and its pathogenesis remains unclear.

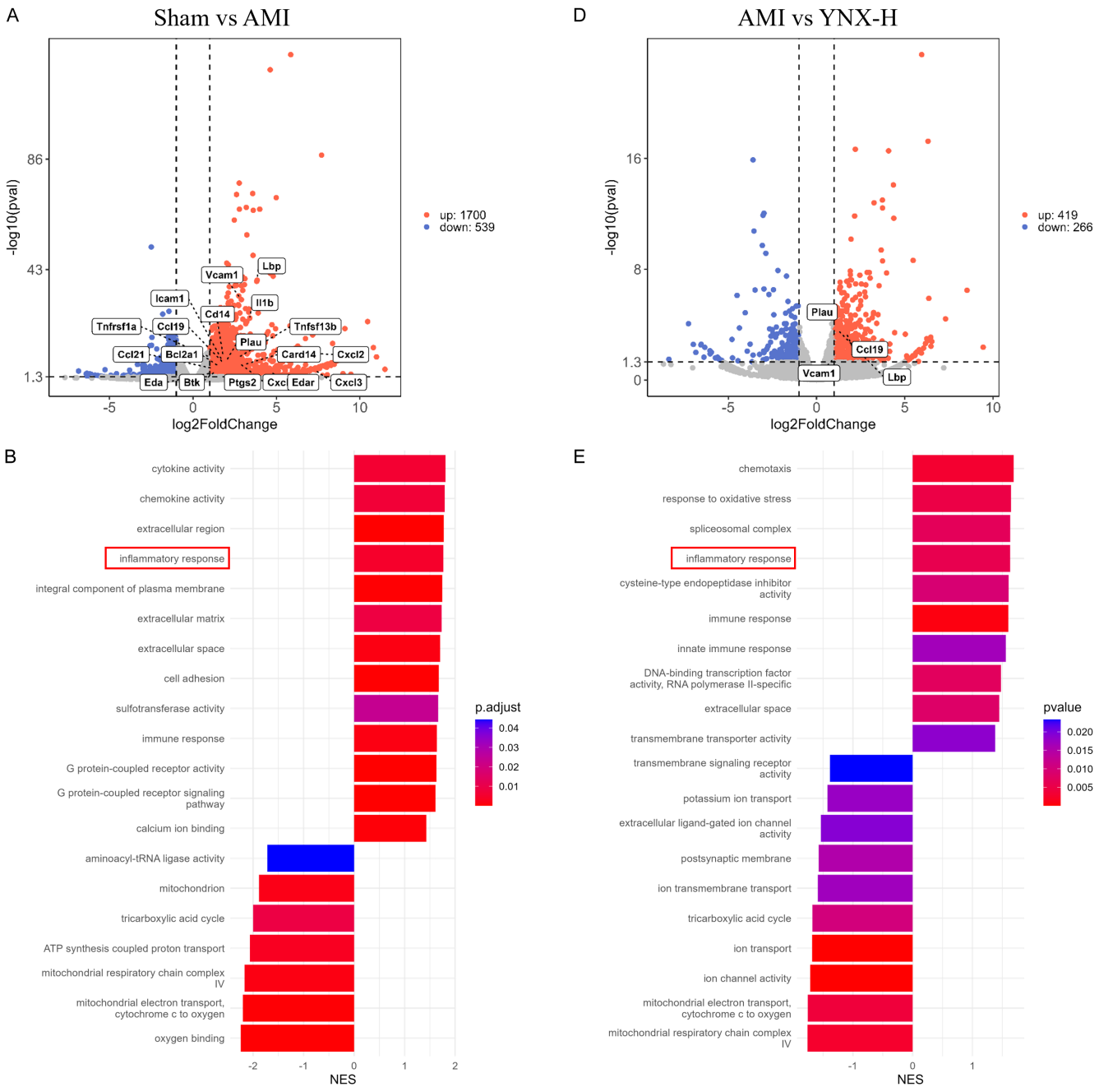
A
Sham vs AMI
-log10(pval)
log2FoldChange
up: 1700
down: 539
Vcam1
Lbp
Icam1
Il1b
Cd14
Tnfrsf1a
Ccl19
Tnfsf13b
Plau
Ccl21
Bcl2a1
Card14
Cxcl2
Eda
Btk
Ptgs2
Cxc
Edar
Cxcl3
D
AMI vs YNX-H
up: 419
down: 266
Plau
Ccl19
Vcam1
Lbp
B
cytokine activity
chemokine activity
extracellular region
inflammatory response
integral component of plasma membrane
extracellular matrix
extracellular space
cell adhesion
sulfotransferase activity
immune response
G protein-coupled receptor activity
G protein-coupled receptor signaling pathway
calcium ion binding
aminoacyl-tRNA ligase activity
mitochondrion
tricarboxylic acid cycle
ATP synthesis coupled proton transport
mitochondrial respiratory chain complex IV
mitochondrial electron transport, cytochrome c to oxygen
oxygen binding
NES
p.adjust
E
chemotaxis
response to oxidative stress
spliceosomal complex
inflammatory response
cysteine-type endopeptidase inhibitor activity
immune response
innate immune response
DNA-binding transcription factor activity, RNA polymerase II-specific
extracellular space
transmembrane transporter activity
transmembrane signaling receptor activity
potassium ion transport
extracellular ligand-gated ion channel activity
postsynaptic membrane
ion transmembrane transport
tricarboxylic acid cycle
ion transport
ion channel activity
mitochondrial electron transport, cytochrome c to oxygen
mitochondrial respiratory chain complex IV
NES
pvalue

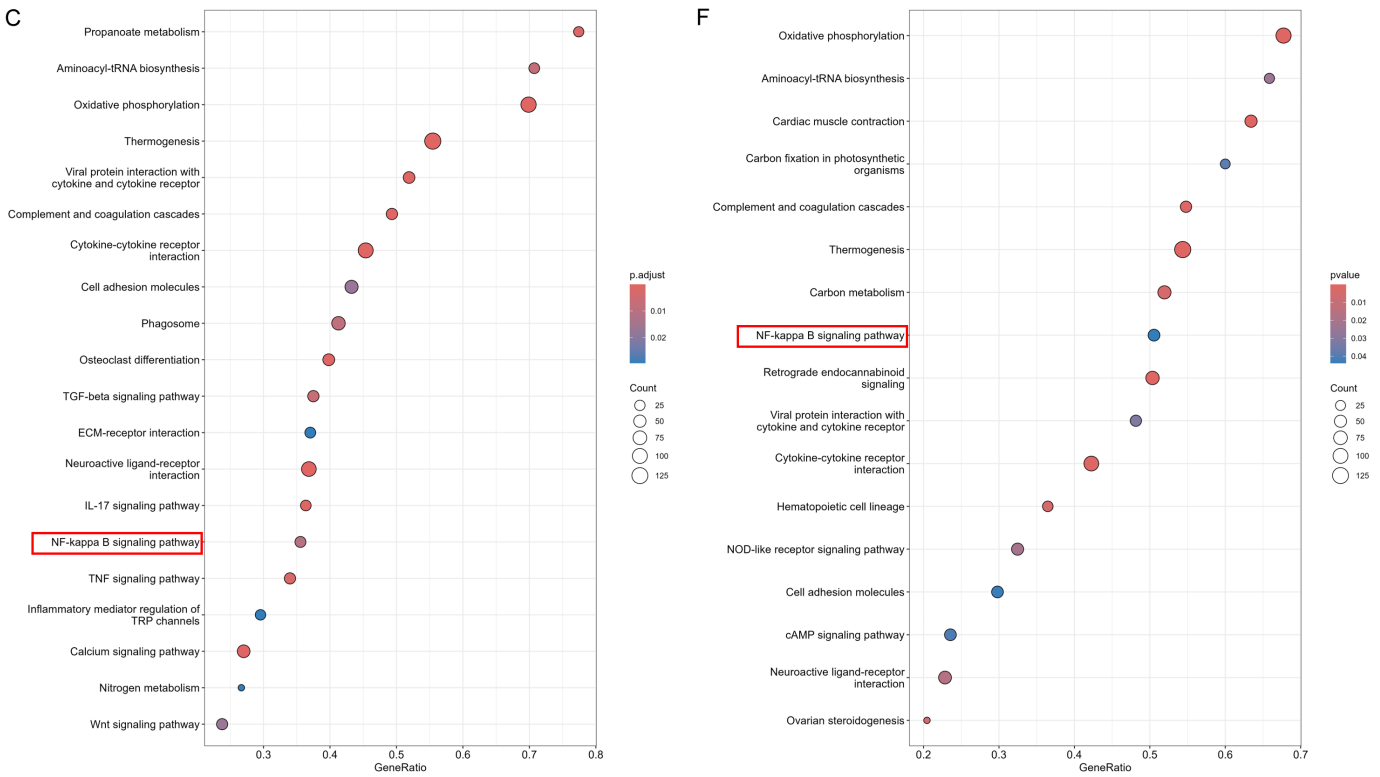

Figure 4. Transcriptomic analysis of DEGs in myocardial tissues from the control, AMI, and YNX groups. A. Volcano plot of DEGs between the AMI and control groups; B. GO enrichment analysis of DEGs between the AMI and control groups; C. KEGG pathway analysis of DEGs between the AMI and control groups; D. Volcano plot of DEGs between the YNX and AMI groups; E. GO enrichment analysis of DEGs between the YNX and AMI groups; F. KEGG pathway analysis of DEGs between the YNX and AMI groups. Notes: DEGs, differentially expressed genes; AMI, acute myocardial infarction; GO, Gene Ontology; KEGG, Kyoto Encyclopedia of Genes and Genomes.

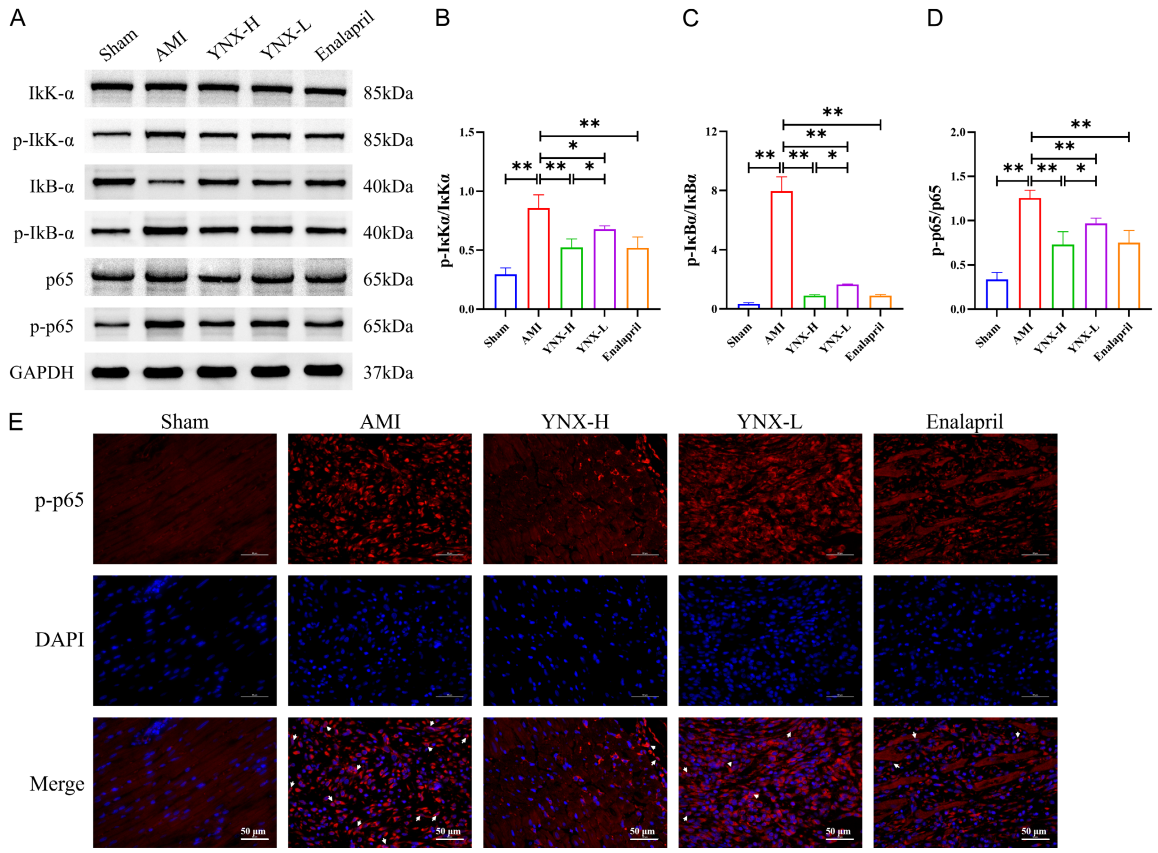

Figure 5. Analysis of NF-κB signaling pathway activation in rat myocardial tissues. A-D. Western blotting and quantitative analysis were performed to evaluate the expression levels of IκKα, p-IκKα, IκBα, p-IκBα, p65, and p-p65 in myocardial tissues across different groups; E. IF staining to visualize the subcellular localization of p-p65 in cardiomyocytes (scale bar = 50 μm). Notes: IκKα, inhibitor of κB kinase α; p-IκKα, phosphorylated IKKα; IκBα, inhibitor of κBα; p-IκBα, phosphorylated IκBα. Data are expressed as mean ± SEM (n = 3). *P<0.05, **P<0.01.

In the present study, several key findings were clarified. First, YNX significantly improved cardiac function and protected against AMI. Second, AMI rats exhibited notably high iron ion accumulation in myocardial tissues, and this ion deposition was significantly attenuated by YNX administration in a dose-dependent manner. Third, transcriptome sequencing and experiment validation suggested that YNX can significantly suppress NF-κB activation compared to the control group, with a stronger inhibitory effect observed in the YNX-H group than in the YNX-L group. Fourth, in an *in vitro* AMI model using H9c2 cells, YNX treatment significantly decreased ROS, MDA, and LDH levels and promoted GSH release. Lastly, the inhibitory effect of YNX in ferroptosis was partially reversed by the ferroptosis activator erastin and an NF-κB activator.

Despite significant advancements in pharmacological and medical device interventions over the past several decades, the incidence of heart failure after myocardial infarction remains high [38, 39]. Therefore, elucidating the precise mechanisms underlying myocardial infarction is essential for developing novel treatments.

In the present study, we investigated the molecular mechanisms by which YNX improves cardiac function in AMI model rats by regulating cardiomyocyte ferroptosis and the NF-κB pathway. We noted that YNX treatment notably decreased LVEDD and LVESD while markedly increasing LVEF and LVFS. Histopathological analysis also confirmed these findings. Masson's trichrome staining revealed that cardiac myofibrosis was relieved in the YNX group compared with the model group. Collectively, these results suggest that YNX improves cardiac contractile function by alleviating myocardial remodeling and fibrosis. Previous studies have revealed that myocardial fibrosis is an essential determinant of cardiac function decline follow-

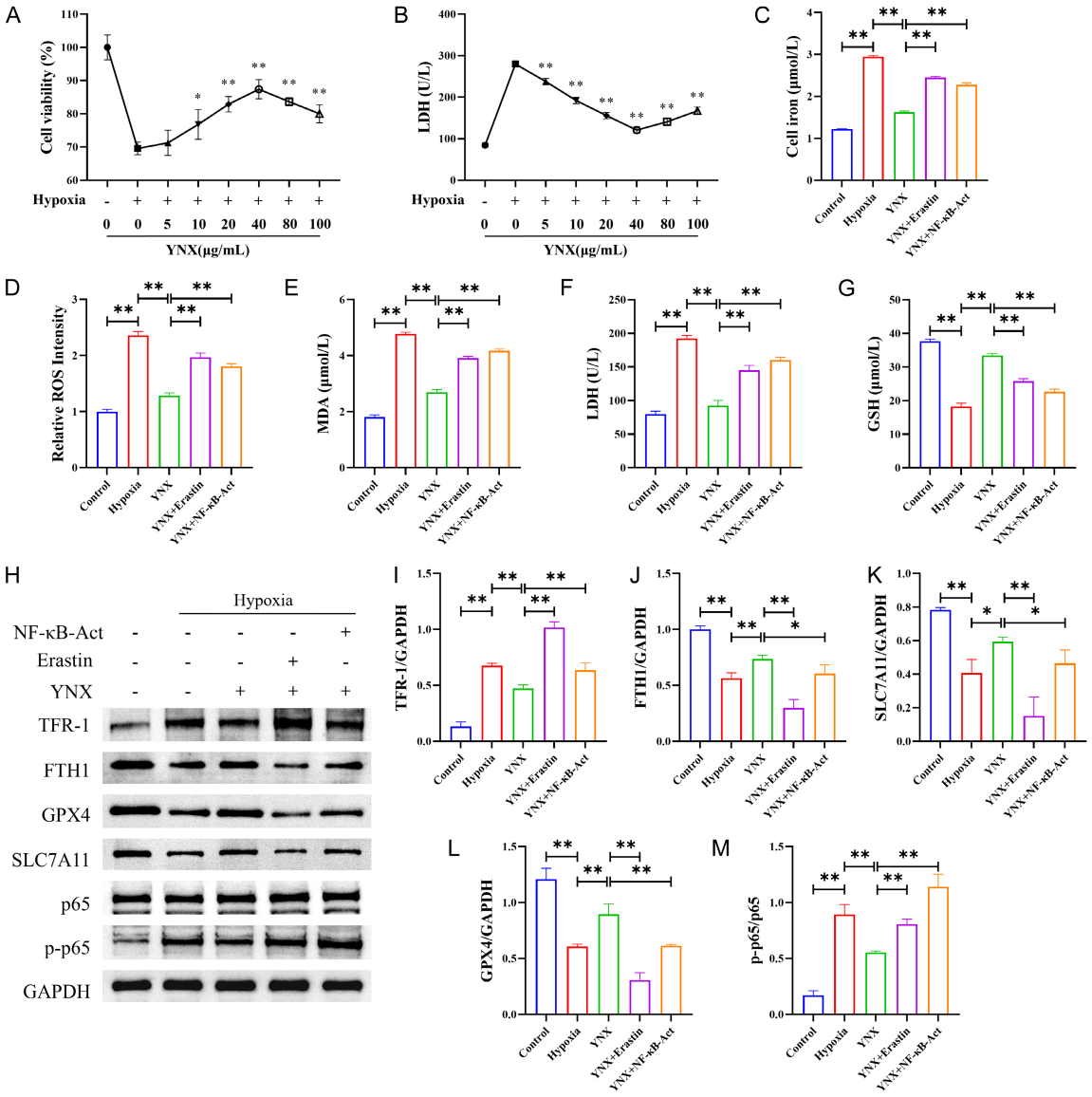

Figure 6. Effects of YNX on AMI in H9c2 cells. A. Effects of varying concentrations of YNX on H9c2 cell viability after hypoxic exposure; B. Effects of various concentrations of YNX on LDH levels in H9c2 cells after hypoxic exposure; C. Intracellular ion concentration in H9c2 cells; D-G. Levels of LDH, GSH, MDA, and ROS in H9c2 cells; H-M. Western blotting and quantitative analysis for evaluation of the expression levels of ferroptosis-related proteins, including TFR-1, FTH1, SLC7A11 and GPX4 as well as p-p65 and p65 in the H9c2 cells. Notes: TFR-1, transferrin receptor-1; FTH1, ferritin heavy chain 1; GPX4, glutathione peroxidase 4; SLC7A11, solute carrier family 7 member 11; LDH, lactate dehydrogenase; MDA, malondialdehyde; SOD, superoxide dismutase; GSH, glutathione. Data are expressed as mean ± SEM (n = 3). **P*<0.05, ***P*<0.01.

ing AMI and that inhibiting fibrosis can effectively slow down the progression of heart failure [40, 41]. Our study provides the experimental basis for the antifibrotic use of YNX.

Ferroptosis, characterized by lipid peroxidation, exerts an essential effect on myocardial injury after AMI [42]. In this study, YNX significantly decreased iron accumulation in the myocardial tissues and serum of AMI model rats. Meanwhile, YNX markedly modulated iron metabolism-related proteins by downregulating TFR-1 levels and upregulating FTH-1, GPX4, and SLC7A11 levels. Combined with the changes in serum oxidative stress indices (decreased LDH and MDA levels and increased SOD and GSH levels), these results suggest that YNX may inhibit iron-induced ferroptosis in myocardial

tissues by alleviating iron overload and suppressing lipid peroxidation. Notably, the protective effect of high-dose YNX was more pronounced than that of low-dose YNX, demonstrating a dose-dependent pattern, which is consistent with the multi-target and multi-pathway therapeutic features of most Chinese natural herbal products (CNHPs) [43, 44].

Transcriptome analysis revealed the significant enrichment of the NF-κB pathway among DEGs between the AMI and YNX-H groups. Western blotting and IF assays further confirmed that YNX markedly inhibited the phosphorylation of key proteins in the NF-κB pathway (e.g., IκKα, IκBα, and p65) and p65 nuclear transport. Excessive NF-κB pathway activation can exacerbate apoptosis and inflammatory responses [45, 46]. Our results provide novel evidence supporting a synergistic effect of the NF-κB pathway and ferroptosis: in the H9c2 cell model, the NF-κB activator reversed the inhibitory effects of YNX on ferroptosis, suggesting that YNX indirectly modulates the levels of iron metabolism-associated proteins by suppressing the NF-κB pathway to inhibit myocardial injury. Therefore, our study provides novel mechanistic insights into AMI treatment and suggests that the NF-κB pathway may serve as an essential hub in the intersection of inflammation and ferroptosis.

In vitro experiments proved that YNX (40 μg/mL) significantly enhanced cell viability, reduced LDH release, and lowered intracellular ROS and MDA levels in H9c2 cells, thereby exerting its anti-ferroptotic effect. However, the ferroptosis activator erastin partially reversed the protective action of YNX, indicating that the cardioprotective mechanism of YNX is closely associated with the ferroptosis pathway. Therefore, the reversal of the anti-apoptotic effect of YNX by an NF-κB activator additionally suggests the important role of the NF-κB pathway in the protective mechanism of YNX.

Despite these encouraging findings, several limitations in this study need to be acknowledged. First, the specific active components of YNX and their corresponding molecular targets have not yet been clearly identified. Second, the roles of NF-κB downstream target molecules in regulating ferroptosis-related proteins, such as GPX4 and SLC7A11, need to be further elucidated. Moreover, the lack of long-term follow-up information limits a comprehensive evaluation of the sustained effect of YNX on cardiac functional outcomes. Future studies should integrate metabolomics to identify the effective components of YNX, apply gene-editing tools, including CRISPR-Cas9, to validate key molecular targets, and conduct preclinical studies for translational application.

Conclusion

YNX markedly attenuated myocardial ferroptosis and fibrosis after AMI by suppressing NF-κB pathway activation while modulating iron metabolism and oxidative stress, thereby enhancing cardiac function. These findings enhance our understanding of the mechanisms by which TCM compounds exert their cardioprotective effects in ischemic heart disease and provide a robust theoretical foundation for the development of novel anti-ferroptotic treatment strategies.

Acknowledgements

This work was supported by the Heilongjiang Postdoctoral Fund (LBH-Z22277).

Disclosure of conflict of interest

None.

Address correspondence to: Jiamei Fu, Department of Cardiovascular Medicine, The First Affiliated Hospital of Heilongjiang University of Chinese Medicine, No. 26, Heping Road, Xiangfang District, Harbin 150040, Heilongjiang, China. E-mail: fjmfjm20252025@163.com

References

[1] Galli M, Niccoli G, De Maria G, Brugaletta S, Montone RA, Vergallo R, Benenati S, Magnani G, D'Amario D, Porto I, Burzotta F, Abbate A, Angiolillo DJ and Crea F. Coronary microvascular obstruction and dysfunction in patients with acute myocardial infarction. Nat Rev Cardiol 2024; 21: 283-298.

[2] Anderson JL and Morrow DA. Acute myocardial infarction. N Engl J Med 2017; 376: 2053-2064.

[3] Del Re DP, Amgalan D, Linkermann A, Liu Q and Kitsis RN. Fundamental mechanisms of regulated cell death and implications for heart disease. Physiol Rev 2019; 99: 1765-1817.

[4] Reed GW, Rossi JE and Cannon CP. Acute myocardial infarction. Lancet 2017; 389: 197-210.

[5] Engstrøm T, Kelbæk H, Helqvist S, Høfsten DE, Kløvgaard L, Holmvang L, Jørgensen E, Pedersen F, Saunamäki K, Clemmensen P, De Backer O, Ravkilde J, Tilsted HH, Villadsen AB, Aarøe J, Jensen SE, Raungaard B and Køber L; DANAMI-3-PRIMULTI Investigators. Complete revascularisation versus treatment of the culprit lesion only in patients with ST-segment elevation myocardial infarction and multivessel disease (DANAMI-3-PRIMULTI): an open-label, randomised controlled trial. Lancet 2015; 386: 665-671.

[6] Keeley EC and Weaver WD. Combination therapy for acute myocardial infarction. J Am Coll Cardiol 1999; 34: 1963-1965.

[7] Lev EI and Ben-Assa E. Dual antiplatelet therapy in patients with prior myocardial infarction: the twilight of prolonged DAPT duration? JACC Cardiovasc Interv 2022; 15: 294-296.

[8] Reddy RK, Howard JP, Jamil Y, Madhavan MV, Nanna MG, Lansky AJ, Leon MB and Ahmad Y. Percutaneous coronary revascularization strategies after myocardial infarction: a systematic review and network meta-analysis. J Am Coll Cardiol 2024; 84: 276-294.

[9] Fang X, Ardehali H, Min J and Wang F. The molecular and metabolic landscape of iron and ferroptosis in cardiovascular disease. Nat Rev Cardiol 2023; 20: 7-23.

[10] Wu X, Li Y, Zhang S and Zhou X. Ferroptosis as a novel therapeutic target for cardiovascular disease. Theranostics 2021; 11: 3052-3059.

[11] Zhang Y, Xin L, Xiang M, Shang C, Wang Y, Wang Y, Cui X and Lu Y. The molecular mechanisms of ferroptosis and its role in cardiovascular disease. Biomed Pharmacother 2022; 145: 112423.

[12] Liu Y, Wan Y, Jiang Y, Zhang L and Cheng W. GPX4: the hub of lipid oxidation, ferroptosis, disease and treatment. Biochim Biophys Acta Rev Cancer 2023; 1878: 188890.

[13] Tang D and Kroemer G. Ferroptosis. Curr Biol 2020; 30: R1292-R1297.

[14] Cruz-Gregorio A, Amezcua-Guerra LM, Fisher-Bautista B, Romero-Beltrán A and Fonseca-Camarillo G. The protective role of interleukin-37 in cardiovascular diseases through ferroptosis modulation. Int J Mol Sci 2024; 25: 9758.

[15] Jin S, Wang H, Zhang X, Song M, Liu B and Sun W. Emerging regulatory mechanisms in cardiovascular disease: ferroptosis. Biomed Pharmacother 2024; 174: 116457.

[16] Wang H, Xie B, Shi S, Zhang R, Liang Q, Liu Z and Cheng Y. Curdione inhibits ferroptosis in isoprenaline-induced myocardial infarction via regulating Keap1/Trx1/GPX4 signaling pathway. Phytother Res 2023; 37: 5328-5340.

[17] Cai J, Wang X, Wang Z, Sheng S, Tang F and Zhang Z. ZC3H13-mediated m6A modification ameliorates acute myocardial infarction through preventing inflammation, oxidative stress and ferroptosis by targeting lncRNA93358. Inflammation 2025; 48: 1270-1284.

[18] Barnabei L, Laplantine E, Mbongo W, Rieux-Laucat F and Weil R. NF-κB: at the borders of autoimmunity and inflammation. Front Immunol 2021; 12: 716469.

[19] Capece D, Verzella D, Flati I, Arboretto P, Cornice J and Franzoso G. NF-κB: blending metabolism, immunity, and inflammation. Trends Immunol 2022; 43: 757-775.

[20] Rius-Pérez S, Pérez S, Martí-Andrés P, Monsalve M and Sastre J. Nuclear factor kappa b signaling complexes in acute inflammation. Antioxid Redox Signal 2020; 33: 145-165.

[21] Wickert A, Schwantes A, Fuhrmann DC and Brüne B. Inflammation in a ferroptotic environment. Front Pharmacol 2024; 15: 1474285.

[22] Zhang H and Sun SC. NF-κB in inflammation and renal diseases. Cell Biosci 2015; 5: 63.

[23] Yan N, Xu Z, Qu C and Zhang J. Dimethyl fumarate improves cognitive deficits in chronic cerebral hypoperfusion rats by alleviating inflammation, oxidative stress, and ferroptosis via NRF2/ARE/NF-κB signal pathway. Int Immunopharmacol 2021; 98: 107844.

[24] Zhao C, Sun G, Li Y, Kong K, Li X, Kan T, Yang F, Wang L and Wang X. Forkhead box O3 attenuates osteoarthritis by suppressing ferroptosis through inactivation of NF-κB/MAPK signaling. J Orthop Translat 2023; 39: 147-162.

[25] Zhang Y, Wu J, Guo S, Lin W, Zhang B, Chen X, Mo H and Zhan T. The clinical efficacy and safety of the Chinese herbal medicine Astragalus (Huangqi) preparation for the treatment of acute myocardial infarction: a systematic review of randomized controlled trials. Medicine (Baltimore) 2019; 98: e15256.

[26] Luo LF, Guan P, Qin LY, Wang JX, Wang N and Ji ES. Astragaloside IV inhibits adriamycin-induced cardiac ferroptosis by enhancing Nrf2 signaling. Mol Cell Biochem 2021; 476: 2603-2611.

[27] Liao JZ, Chai ZN, Li WS, Liu XF, Wang S, Qin L and Guo WQ. Pharmacologic effects of codonopsis pilosula-astragalus injection in the treatment of CHD patients. J Tradit Chin Med 1988; 8: 1-8.

[28] Fu D, Zhou J, Xu S, Tu J, Cai Y, Liu J, Cai Z and Wang D. Smilax glabra Roxb. flavonoids protect against pathological cardiac hypertrophy by inhibiting the Raf/MEK/ERK pathway: In vivo and in vitro studies. J Ethnopharmacol 2022; 292: 115213.

[29] Song X, Kong J, Song J, Pan R and Wang L. Angelica sinensis polysaccharide alleviates myocardial fibrosis and oxidative stress in the heart of hypertensive rats. Comput Math Methods Med 2021; 2021: 6710006.
[30] Tang Z, Cheng L, Li M, Chen J and Huang C. Astragaloside IV alleviates osteoarthritis by inhibiting chondrocyte ferroptosis via the p53/SLC7A11/GPX4 axis. J Inflamm Res 2025; 18: 16169-16186.
[31] Zou YF, Li CY, Fu YP, JiZe XP, Zhao YZ, Peng X, Wang JY, Yin ZQ, Li YP, Song X, Li LX, Zhao XH, Feng B, Huang C, Ye G, Tang HQ, Chen J, Li R, Chen XF and Tian ML. Angelica sinensis aboveground part polysaccharide and its metabolite 5-MT ameliorate colitis via modulating gut microbiota and TLR4/MyD88/NF-κB pathway. Int J Biol Macromol 2023; 242: 124689.
[32] Chen Z, Shi Q, Liu X, Lu G, Yang J, Luo W and Yang F. Codonopsis radix inhibits the inflammatory response and oxidative stress in chronic obstructive pulmonary disease mice through regulation of the Nrf2/NF-κB signaling pathway. Pharmacology 2024; 109: 266-281.
[33] Cao X, Zhou M, Liu H, Chen X, Li X and Jia S. Clinical efficacy and safety of shensong yangxin capsule-amiodarone combination on heart failure complicated by ventricular arrhythmia: a meta-analysis of randomized controlled trials. Front Pharmacol 2021; 12: 613922.
[34] Lu X, Wang T, Hou B, Han N, Li H, Wang X, Xin J, He Y, Zhang D, Jia Z and Wei C. Shensong yangxin, a multi-functional traditional Chinese medicine for arrhythmia: a review of components, pharmacological mechanisms, and clinical applications. Heliyon 2024; 10: e35560.
[35] Yu XH, Yu XW, Xu ZM and Li HX. Yangxin decoction for the treatment of angina pectoris of coronary heart disease: a systematic review of randomized controlled trial. Medicine (Baltimore) 2022; 101: e30394.
[36] Peng Y, Liao B, Zhou Y, Zeng W and Zeng ZY. Atorvastatin inhibits ferroptosis of H9C2 cells by regulatingSMAD7/Hepcidin expression to improve ischemia-reperfusion injury. Cardiol Res Pract 2022; 2022: 3972829.
[37] Zhang W, Liu K, Ren GM, Wang Y, Wang T, Liu X, Li DX, Xiao Y, Chen X, Li YT, Zhan YQ, Xiang SS, Chen H, Gao HY, Zhao K, Yu M, Ge CH, Li CY, Ge ZQ, Yang XM and Yin RH. BRISC is required for optimal activation of NF-κB in Kupffer cells induced by LPS and contributes to acute liver injury. Cell Death Dis 2023; 14: 743.
[38] Udell JA, Jones WS, Petrie MC, Harrington J, Anker SD, Bhatt DL, Hernandez AF and Butler J. Sodium glucose cotransporter-2 inhibition for acute myocardial infarction: JACC review topic of the week. J Am Coll Cardiol 2022; 79: 2058-2068.
[39] Usman MS, Bhatt DL, Hameed I, Anker SD, Cheng AYY, Hernandez AF, Jones WS, Khan MS, Petrie MC, Udell JA, Friede T and Butler J. Effect of SGLT2 inhibitors on heart failure outcomes and cardiovascular death across the cardiometabolic disease spectrum: a systematic review and meta-analysis. Lancet Diabetes Endocrinol 2024; 12: 447-461.
[40] Prabhu SD and Frangogiannis NG. The biological basis for cardiac repair after myocardial infarction: from inflammation to fibrosis. Circ Res 2016; 119: 91-112.
[41] Yao H, He Q, Huang C, Wei S, Gong Y, Li X, Liu W, Xu Z, Wu H, Zheng C and Gao Y. Panaxatriol saponin ameliorates myocardial infarction-induced cardiac fibrosis by targeting Keap1/Nrf2 to regulate oxidative stress and inhibit cardiac-fibroblast activation and proliferation. Free Radic Biol Med 2022; 190: 264-275.
[42] Zhang CH, Yan YJ and Luo Q. The molecular mechanisms and potential drug targets of ferroptosis in myocardial ischemia-reperfusion injury. Life Sci 2024; 340: 122439.
[43] Li J, Ma A, Lan W and Liu Q. Platycodon D-induced A549 cell apoptosis through RRM1-regulated p53/VEGF/ MMP2 pathway. Anticancer Agents Med Chem 2022; 22: 2458-2467.
[44] Qi Y, Zhou N, Jiang Q, Wang Z, Zhang Y, Li B, Xu W, Liu J, Wang Z and Zhu L. Dose-dependent variation of synchronous metabolites and modules in a Yin/Yang transformation model of appointed ischemia metabolic networks. Front Neurosci 2021; 15: 645185.
[45] Dang X, He B, Ning Q, Liu Y, Guo J, Niu G and Chen M. Alantolactone suppresses inflammation, apoptosis and oxidative stress in cigarette smoke-induced human bronchial epithelial cells through activation of Nrf2/HO-1 and inhibition of the NF-κB pathways. Respir Res 2020; 21: 95.
[46] Ren Q, Guo F, Tao S, Huang R, Ma L and Fu P. Flavonoid fisetin alleviates kidney inflammation and apoptosis via inhibiting Src-mediated NF-κB p65 and MAPK signaling pathways in septic AKI mice. Biomed Pharmacother 2020; 122: 109772.